Electronic Supplementary Material (ESI) for Nanoscale.
This journal is © The Royal Society of Chemistry 2020

The missing pieces of the PuO_2 nanoparticles puzzle

Evgeny Gerber[a,b,c], Anna Yu. Romanchuk[c], Ivan Pidchenko[a,b], Lucia Amidani[a,b], Andre Rossberg[a,b], Christoph Hennig[a,b], Gavin Vaughan[d], Alexander Trigub[e], Tolganay Egorova[c], Stephen Bauters[a,b], Tatiana Plakhova[c], Myrtille O.J.Y. Hunault[f], Stephan Weiss[b], Sergei M. Butorin[g], Andreas C. Scheinost[a,b], Stepan N. Kalmykov[c,e] and Kristina O. Kvashnina*[a,b,c]

---

[a] *The Rossendorf Beamline at ESRF – The European Synchrotron, CS40220, 38043 Grenoble Cedex 9, France.*
[b] *Helmholtz Zentrum Dresden-Rossendorf (HZDR), Institute of Resource Ecology, PO Box 510119, 01314, Dresden.*
[c] *Lomonosov Moscow State University, Department of Chemistry, 119991 Moscow, Russia.*
[d] *ESRF – The European Synchrotron, CS40220, 38043 Grenoble Cedex 9, France.*
[e] *National Research Centre "Kurchatov Institute", 123182 Moscow, Russia.*
[f] *Synchrotron SOLEIL, L'Orme des Merisiers, Saint Aubin BP 48, 91192 Gif-sur-Yvette, France.*
[g] *Molecular and Condensed Matter Physics, Department of Physics and Astronomy, Uppsala University, P.O. Box 516, Uppsala, Sweden.*

Supplementary information

Table of contents

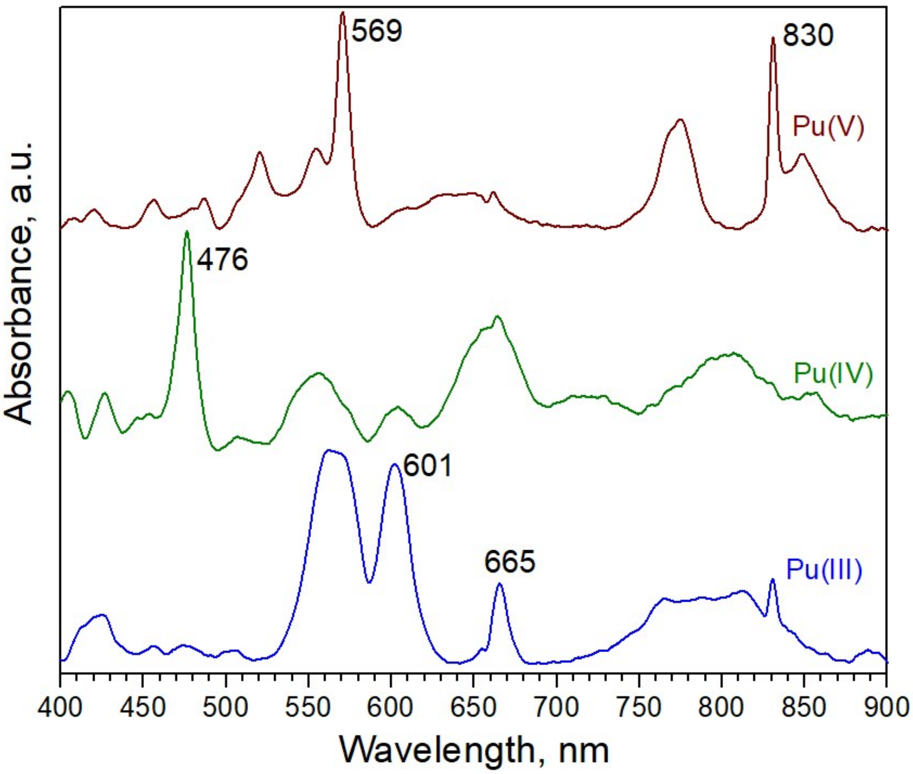

Fig. S1. UV-vis spectra of Pu initial solutions with wavelengths of the characteristic peaks.

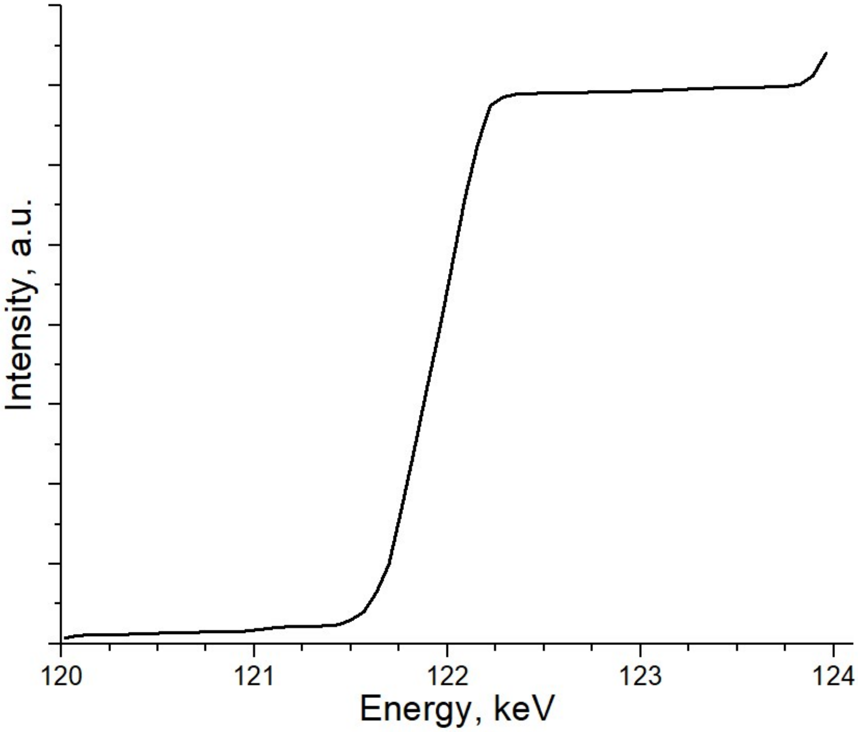

Fig. S2. Pu K-edge XANES spectrum.

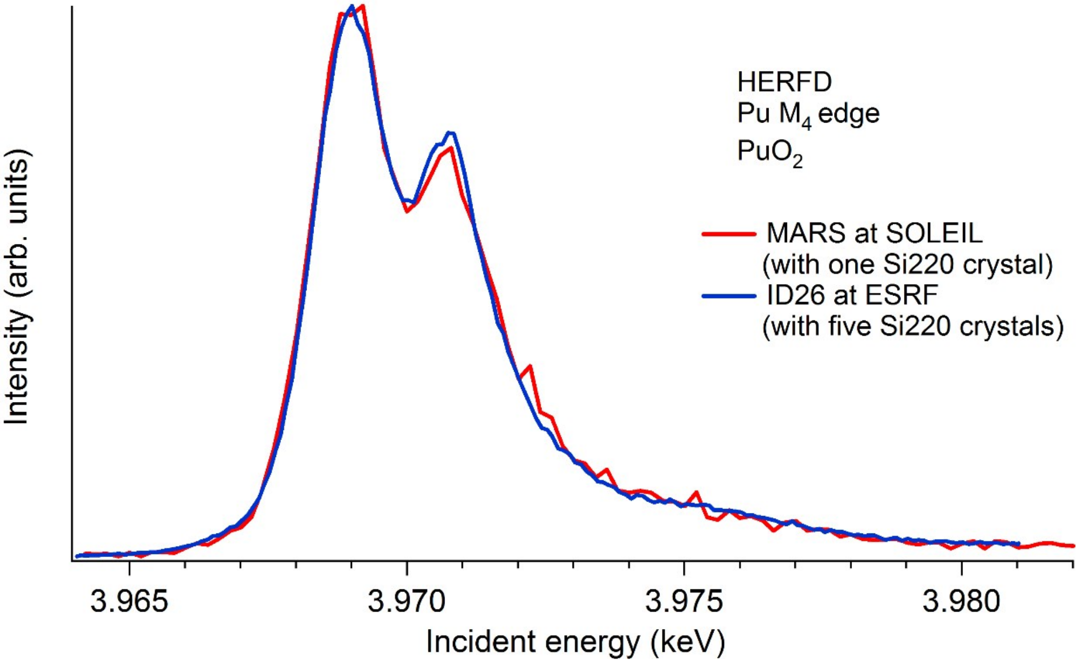

Fig. S3 Comparison of Pu M_4 HERFD data of PuO_2 reference recorded at 2 beamlines: MARS (with single spherically bent Si(220) crystal analyzer) and ID26 beamlines (with five spherically bent crystals analyzers)

```
*  Pu L3 edge
 EDGE      L3
 S02       1.0
 UNFREEZEF
 MULTIPOLE 2 0

 *         pot    xsph  fms   paths genfmt ff2chi
 CONTROL   1      1     1     1     1      1
 PRINT     1      0     0     0     0      0

                          *** ixc=0 means to use Hedin-Lundqvist
 *         ixc  [ Vr  Vi ]
  EXCHANGE  0 0 -1.0

                          *** Radius of small cluster for
                          *** self-consistency calculation
                          *** A sphere including 2 shells is
                          *** a good choice
                          *** l_scf = 0 for a solid, 1 for a molecule
 *         r_scf  [ l_scf   n_scf   ca ]
 SCF       4.0      0       50      0.05   10

                          *** Upper limit of XANES calculation.
                          *** This *must* be uncommented to
                          *** make Feff calculate full multiple
                          *** scattering rather than a path expansion
 *         kmax   [ delta_k  delta_e ]
 XANES     8.0
                          *** Radius of cluster for Full Multiple
                          *** Scattering calculation
                          *** l_fms = 0 for a solid, 1 for a molecule
 *         r_fms     l_fms
 FMS       12        0

                          *** Energy grid over which to calculate
                          *** DOS functions
 *         emin  emax   eimag
 LDOS      -30   20     0.1

                          *** for EXAFS:  RMAX   6.0 and uncomment
                          *** the EXAFS card
 RPATH     0.1
 *EXAFS     20

 POTENTIALS
 *   ipot   Z  element        l_scmt  l_fms   stoichiometry
     0     94     Pu            3       3       0.001
     1     94     Pu            3       3       1
     2     8      O             1       1       2
```

Fig S4. Feff input file for the calculation of Pu L$_3$ HERFD spectrum.

HRTEM. Regardless of conditions and pH, similar nanoparticles containing Pu and O are formed according to the HRTEM data (Fig. 2, Fig S7-8). In all cases, they are aggregates of small crystalline particles with a structure similar to PuO_2. The average particle size is in the range of 2.3-3.2 nm by analysing 40-100 particles in each sample. Size distribution analysis was hampered by the fact that NPs stay in aggregates and size detection of single NPs was not straightforward.

X-ray diffraction. All XRD patterns from nanoparticles are shown in Fig. S5. All diffractograms show similar features and are consistent with the bulk PuO_2 structure. This is in agreement with the HRTEM results. All peaks observed in the PuO_2 reference diffractogram are present in the patterns of the samples. However, these peaks are much broader due to the nanoscale size of the crystallites. To determine the particle size, Scherrer's equation was used:

$$d = \frac{K\lambda}{\beta cos\theta},$$

where d is the mean size of the ordered domains, K – dimensionless shape factor (Scherrer's constant) – 0.9 for spherical NPs, λ – X-ray wavelength, β – the line broadening at half the maximum intensity (FWHM) in radians, θ is the Bragg angle. The calculation of crystallite size was based on the FWHM of the selected peaks, for each sample, at least six selected peaks were used. It is known, that other factors besides crystallite size (*e.g.* microstrain) may cause peak broadening, however, they were not taken into account in our approximation.

The PuO_2 nanocrystals that we obtained from the different starting solutions (more details in Methods) are in a narrow size range of 1.6-2.4 nm estimated by Scherrer's equation. The size of the PuO_2 particles may vary from less than 2 nm up to several hundred nm depending on the synthesis conditions.[1–3] The main factors influencing the size of the nanoparticles are temperature, calcination and the synthesis method. There is a clear tendency in increasing particle size as a function of calcination temperature, from few nanometers to micrometric crystals at approx. 1000°C.[2,4] The smallest particles are synthesized from aqueous solutions, either by adding a base to the acidic plutonium solution (and vice versa)[1,5–7] or by simple water dilution of a concentrated plutonium solution.[5,8] Another powerful method to obtain PuO_2 crystallites of 2-4 nm is a hydrothermal decomposition of plutonium oxalates.[9–12] Firing of the samples leads to the increase of the nanograin size.[11,12] Hydrothermal route and oxalate decomposition are also used to obtain ThO_2 and UO_2 nanoparticles.[13,14] Nanoparticles with an average crystallite size of 2 nm can be obtained by the multi-step thermal decomposition up to 280 °C in a mixture of benzyl ether, oleic acid and oleylamine.[15] Another way to obtain nanoparticles is the sonochemical treatment of PuO_2 suspensions in pure water which results in nanocrystals with an average size of 7 nm.[8] It was also shown that the size of the particles depends on the duration and intensity of the heating (both during and after the synthesis process).[2] However, ageing, which plays a role

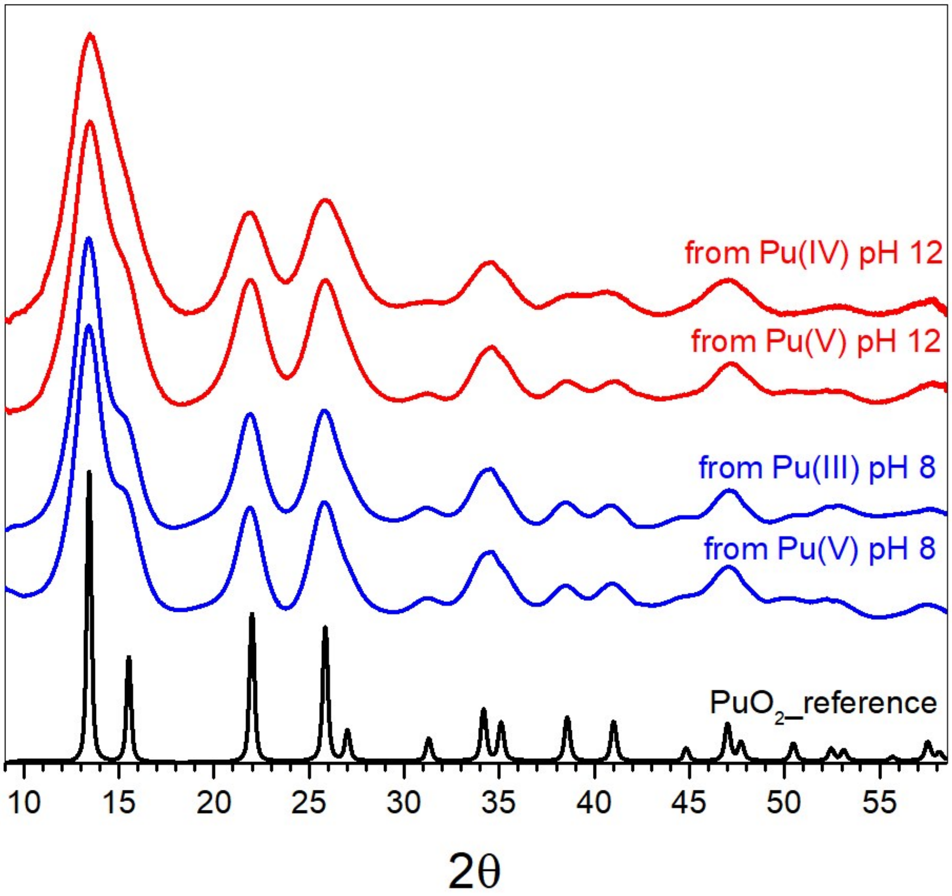

Fig. S5. Diffraction patterns of the precipitates from Pu (III), (IV), (V) in different pH and microcrystalline PuO_2 reference.

in the conversion of particles to the crystalline state, does not discernibly increase the particle size.[1] Fig. S6 shows the correlation between the lattice parameter of PuO_2 nanoparticles and the particle size from our syntheses with data from literature.[1–3,15,16] It should be noted that this dependency is uncertain for small particles as the errors are too large to reveal any significant relation. For larger particles (from 10 nm up to 300 nm) it is apparent that the lattice parameter decreases with increasing particle sizes. The same trend was found for CeO_2 nanoparticles.[17] Hashke et al. reported that the lattice parameter of the PuO_{2+x} changes as a function of x. It is increasing with the O/Pu ratio.[18]

Despite of the small size of the nanoparticles, our reported lattice parameter only differs slightly from PuO_2 bulk (Table 1), meaning that the plutonium from the initial aqueous solutions transfers to a PuO_2-like structure with a clear prevailing Pu(IV) oxidation state. However, there is an equilibrium between several oxidation states in the aqueous solution for the intrinsic colloid formation. Neck and Kim[19] found that the solubility of Pu(IV) oxygen compounds is extremely low. One can suppose that PuO_2 forming from Pu(IV) in solution may shift the equilibrium towards additional Pu(IV) formation and finally lead to PuO_2 as the dominating product in the solid phase. Moreover, as there is no significant difference between XRD data, one can conclude that neither initial oxidation state nor pH affects the PuO_2 structure.

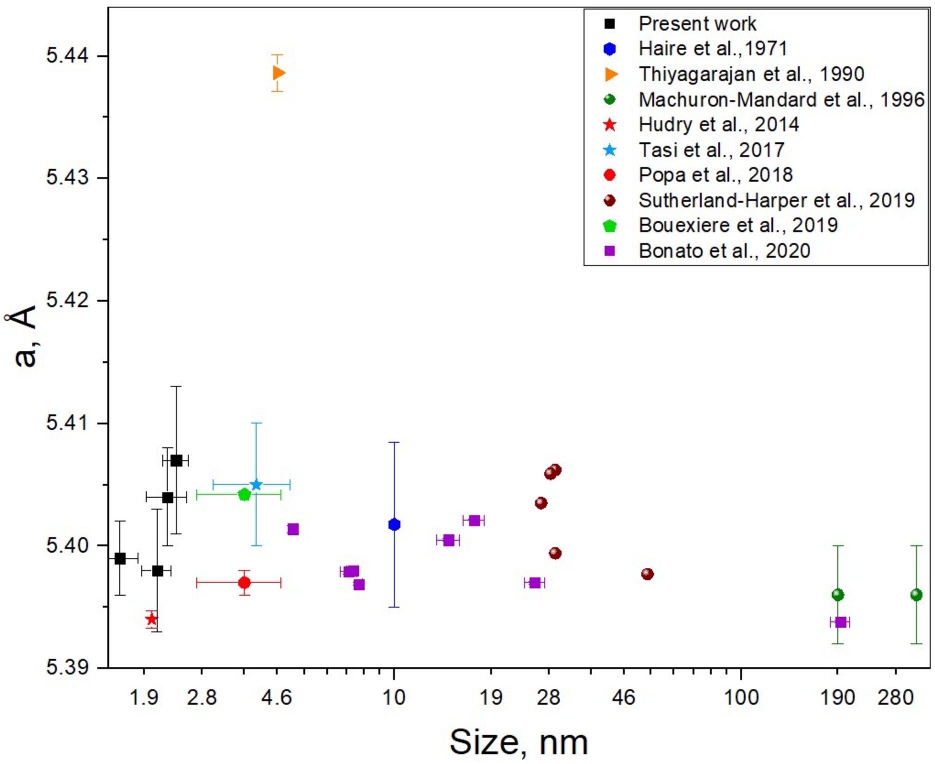

Fig. S6. Lattice parameter distribution of the particle size based on experimental and literature data.[1–3,10–12,15,20]

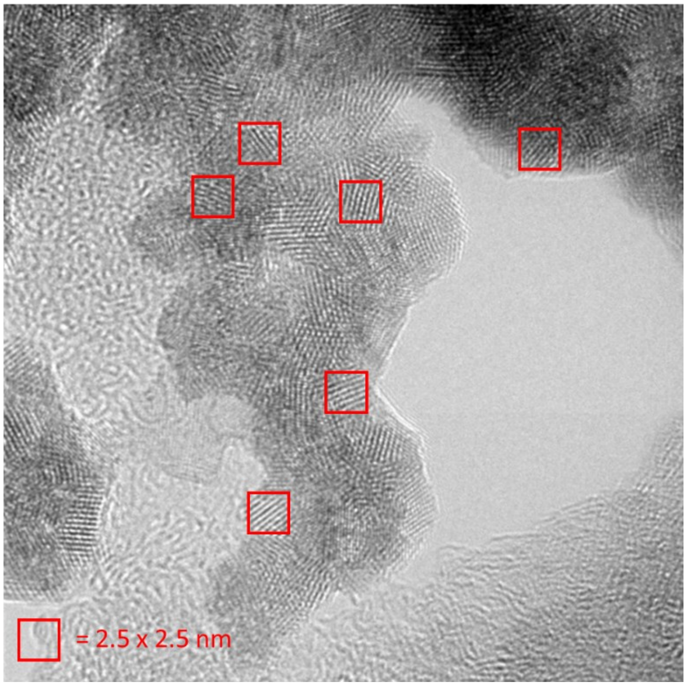

Fig. S7. Size information of PuO_2 NPs. HRTEM image of NPs from Pu(V) pH 8.

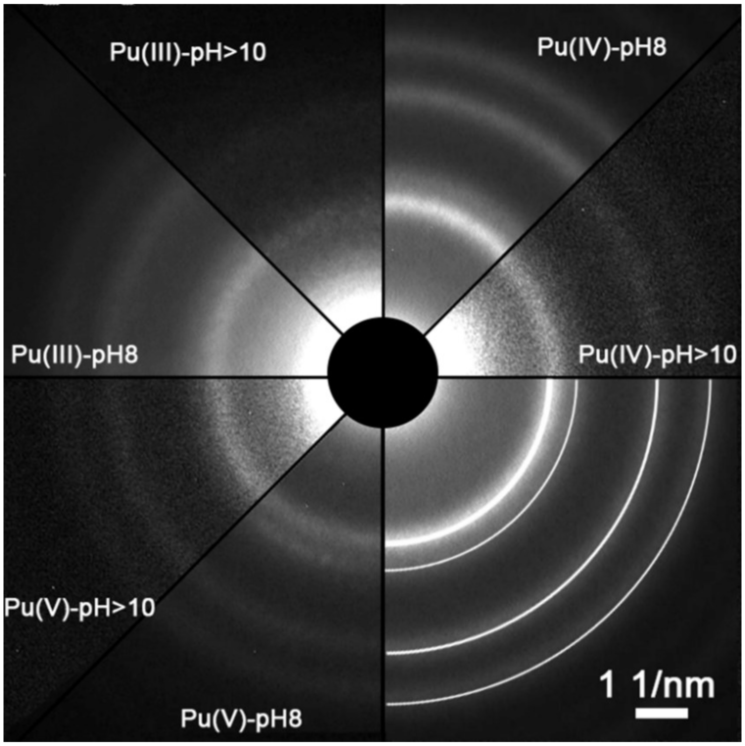

Fig. S8. Structure information of PuO_2 NPs. Selected-area electron diffraction (SAED) patterns of particles, white lines indicate peak positions for PuO_2 standard.

High energy X-ray scattering. The results of the full profile structural refinement are shown in Fig. S9 for all NP samples and the PuO_2 bulk. PuO_2 (space group Fm$\bar{3}$m) was used as a structural model. Water model was used in order to reproduce the contribution of water at the short-range order. The NPs fits are in a good agreement with the PuO_2 structure and the refined parameters are listed in Table S1.

It should be noted that there is only one peak (at 2.31 Å) corresponding to the first shell Pu-O contribution, very similar to the one in PuO_2 bulk. The HEXS results do not show any presence of contributions other than of the Pu-O bond from PuO_2 bulk.

Table S1. The refined parameter values obtained from HEXS.

Sample	Scale factor	a, Å	Particle diameter, nm	Rw
from Pu(III) pH >10	0.81	5.384(6)	1.33(5)	0.20
from Pu(IV) pH >10	0.55	5.38(2)	1.3(2)	0.29
from Pu(V) pH >10	0.64	5.388(5)	1.75(8)	0.23
from Pu(III) pH 8	0.30	5.402(4)	2.07(8)	0.18
from Pu(IV) pH 8	0.44	5.39(2)	1.5(2)	0.32
from Pu(V) pH 8	0.51	5.39(1)	1.7(2)	0.25
PuO_2 reference	0.65	5.4032(3)	-	0.11

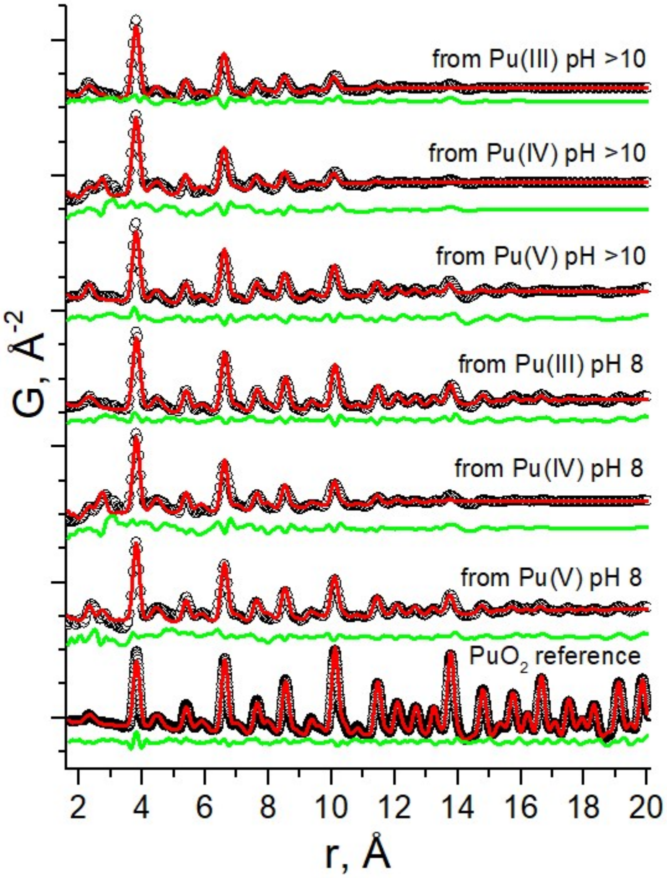

Fig S9. The results of the pair distribution functions (PDFs) fits from all samples and PuO_2 reference. The experimental reduced (PDFs) G(r) obtained by Fourier transformation (FT) of the data with Q_{max} = 26.0 Å^{-1} (black dots), calculated PDFs from the refined structural model (red line) and the difference curve (green line).

HERFD

The Pu L_3 absorption edge refers to the minimum energy needed to excite a core 2*p* electron to the empty Pu 6*d* states. The position and shape of the white line WL gives information about the formal valence. One can see that the WL is the same for all samples and the PuO_2 reference which means the dominating oxidation state for all samples is Pu(IV). However, a minor energy shift among the samples (within 0.5 eV) is observed, and this is most likely the temperature dependence causes such kind of the shift. However, we cannot claim that other oxidation states are not present in tiny (<5%) amounts. Nevertheless, all other spectral features (pre- and post-edge) are corresponding to those of the PuO_2 reference and are perfectly reproduced in the PuO_2 calculated spectra (Fig. 3), thus one can conclude the local environment of all samples is similar to PuO_2. This is also proven with the comparison of the parameters of the WL such as the area under it and FWHM, as seen in Table S2.

The main method to calculate the local density of states (LDOS) is Density Functional Theory (DFT) where either band structure, multiple scattering or chemical DFT codes can be used. FEFF program[21] was used to calculate LDOS and the X-ray

Table S2. Gauss fit results of the WL for the samples.

Sample	Area, (± 1)	FWHM, eV
from Pu(III) pH >10	14	13.0
from Pu(IV) pH >10	13	12.7
from Pu(V) pH >10	13	12.6
from Pu(III) pH 8	14	12.7
from Pu(IV) pH 8	13	13.0
from Pu(V) pH 8	13	12.7
PuO_2 reference	14	13.0

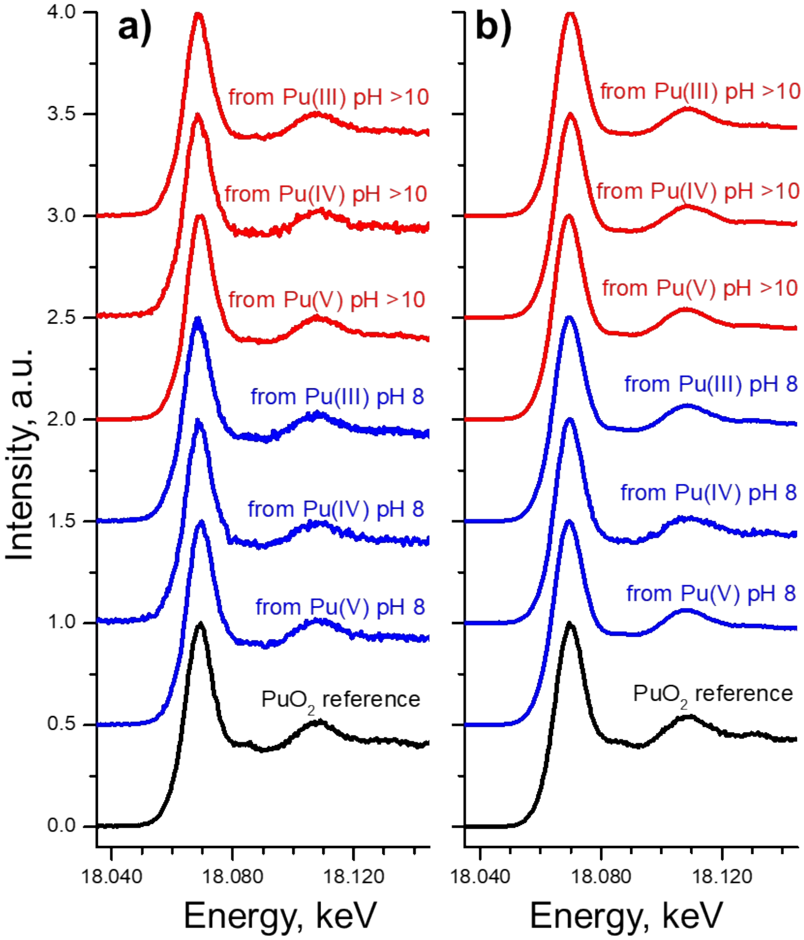

Fig. S10. The normalized HERFD-XANES experimental spectra at the Pu L_3 edge of all samples compared to PuO_2 measured in January (a) and April (b).

absorption spectrum for the PuO_2 cluster. The X-ray absorption spectrum is often related to the density of unoccupied electronic states of the system and one has to calculate the distribution of these unoccupied states in the final state. Pu L_3 edge is probing d-states which are hybridized in our systems. Quadrupole transitions (from 2p to 5f) can be a part of the pre-edge feature as f-states are constituent to the pre-edge part of the spectrum, but these transitions have very low intensity and are not resolved with our resolution.

EXAFS. EXAFS data analysis was based on standard least-squares curve fitting using the ATHENA[22] and the WinXAS[23] program packages. The EXAFS was extracted from the spectra by using a polynomial spline function to approximate the smooth atomic absorption. E_0, the origin for calculating the EXAFS $\chi(k)$-function is fixed at the white line - peak maximum in the XAFS spectra at ~ 18062 eV. Metric parameters (neighbouring atomic distances R_i, EXAFS Debye-Waller factors σ^2_i and coordination numbers N_i for the different coordination shells i) are determined using the FEFFIT code. All shell fits were carried out in R-space of k^3 -weighted spectra (Fourier transformed (FT) over a k-range of ~2.0 – 14 $Å^{-1}$) using theoretical backscattering amplitudes and phase shifts calculated with FEFF 8.2[24,25] on clusters (R_{max} = 8 Å) derived from the structure of PuO_2.[26] The amplitude reduction factor S_0^2 was fixed at 0.95. Debye-Waller factors were restricted to float between 0.001 and 0.010 $Å^2$.

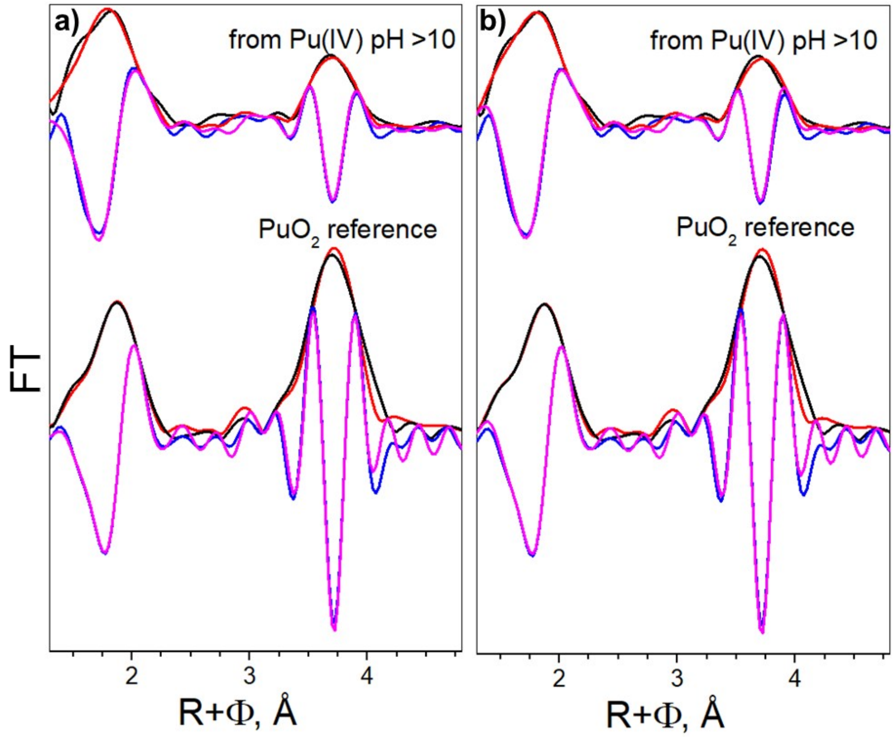

Fig. S11. R-space EXAFS fit results. k-range of 2.0-14.0 $Å^{-1}$, fit range R+Φ 1.30-4.50 Å. Fourier transform of experimental data: magnitude (black) and imaginary part (blue). FT of fit: magnitude (red) and imaginary part (pink). Fit results for two (a) and three (b) oxygen scattering paths, respectively.

Keeping in mind previous reports,[12,15,27,28] we performed additional fittings of EXAFS spectra using different approaches. The “three shell fit” approach considers three different Pu-O interactions in total: Pu(V)-O, Pu(IV)-O and Pu(IV)-OH (or, more generally, the oxygen atom with different coordination in comparison with Pu(IV)-O). The “two shell fit” approach excludes the Pu(V)-O scattering path, hence only two different paths remain. The fit obtained for the reference and one nanoparticle sample are shown in Fig. S11. Fit results of the other samples are reported in Table S3-S4 and Fig. 4a.

Three shell fit: The resulting fits obtained for all samples have only a slight parameter distribution (Table S3). The average distances are $R_{Pu(V)-O}$ - 1.83 Å, $R_{Pu(IV)-OH}$ – 2.28 Å, $R_{Pu(IV)-O}$ – 2.43 Å with coordination numbers 0.3, 4.8 and 1.9 respectively. However, if the first scattering path is ascribed as PuO_2^+, the CN of O would be 2 for pure Pu(V). it assumes the amount of Pu(V) reaches up to 15% ($CN_{Pu(V)-O}/2$, where 2 is the coordination number of oxygen in case of pure Pu(V) as the PuO_2^+ cation) among all Pu present, which would definitely appear in the HERFD-data. In addition, the fit with three scattering paths was also obtained for the annealed reference sample, where we do not expect any detectable amounts of Pu(V) chemically, however, the fit of this standard appears unstable.

Table S3. Parameters extracted by least-squares fit analysis of Pu L_3 EXAFS spectra with three O shells (k-range of 2.0-14.0 Å^{1})*.

Sample	Coordination shell									ΔE_0 [eV]	$\chi^2_{res\,\%}$
	First O shell			Second O shell			Third O shell				
	CN	R [Å]	σ^2 [Å^2]	CN	R [Å]	σ^2 [Å^2]	CN	R [Å]	σ^2 [Å^2]		
from Pu(III) pH >10	0.4	1.83	0.0010	4.0	2.29	0.0035	1.8	2.43	0.0010	7.6	14.2
from Pu(IV) pH >10	0.2	1.85	0.0010	5.5	2.29	0.0068	1.5	2.44	0.0027	6.8	10.3
from Pu(V) pH >10	0.2	1.84	0.0010	4.8	2.28	0.0052	2.2	2.42	0.0025	6.4	9.2
from Pu(III) pH 8	0.2	1.82	0.0010	4.4	2.28	0.0049	2.3	2.42	0.0025	6.3	11.5
from Pu(IV) pH 8	0.2	1.81	0.0010	6.1	2.28	0.0083	1.6	2.42	0.0022	5.6	8.77
from Pu(V) pH 8	0.5	1.84	0.0010	3.7	2.29	0.0032	2.1	2.44	0.0053	8.4	18.7
PuO_2 reference	0.7	1.89	0.0100	2.1	2.24	0.004	6.3	2.35	0.0040	6.8	9.3

*CN: Coordination number with error ± 25 %, R: Radial distance with error ± 0.01 Å, σ^2: Debye-Waller factor with error ±0.0005 Å^2.

Two shell fit: All parameters of the second approach fit are listed in the Table S4. One can see that the distribution of distances and coordination numbers is larger than in the previous approach, which may be an indirect evidence that the fit is more unstable. Nevertheless, two components can be extracted and assigned as Pu-OH and Pu-O scattering paths. However, despite of improving the EXAFS fit with additional contributions in the first coordination shell, the situation remains again unclear as the same fit could be performed for the reference PuO_2 sample, though this additional path cannot be used for this sample as there should not be any Pu-OH bonds, only Pu-O.

Table S4. Parameters extracted by least-squares fit analysis of Pu L_3 EXAFS spectra with two O shells (k-range of 2.0-14.0 Å^{-1})*.

Sample	Coordination shell						ΔE_0 [eV]	$\chi^2_{res\,\%}$
	First O shell			Second O shell				
	CN	R [Å]	σ^2 [Å^2]	CN	R [Å]	σ^2 [Å^2]		
from Pu(III) pH >10	7.4	2.30	0.0097	0.6	2.44	0.0010	5.4	16.8
from Pu(IV) pH >10	6.1	2.28	0.0081	1.9	2.42	0.0043	5.4	11.5
from Pu(V) pH >10	6.5	2.29	0.0080	1.5	2.42	0.0025	5.2	9.9
from Pu(III) pH 8	7.2	2.29	0.0096	0.8	2.43	0.0010	4.9	12.8
from Pu(IV) pH 8	5.7	2.26	0.0076	2.3	2.41	0.0030	4.7	13.0
from Pu(V) pH 8	5.5	2.26	0.0076	2.5	2.39	0.0032	3.9	22.4
PuO_2 reference	6.0	2.30	0.0059	2.0	2.38	0.0021	6.44	10.4

*CN: Coordination number with error ± 25 %, R: Radial distance with error ± 0.01 Å, σ^2: Debye-Waller factor with error ±0.0005 Å^2.

To confirm or refute this approach, additional proof is needed while we used the exemplary sample with Pu(IV) at pH >10. In order to clarify the approach, we established a theoretical EXAFS spectrum simulation for PuO_2. We started from EXAFS Landweber iteration (LI),[29,30] which is used to construct the radial particle distribution function (n(r)) from an EXAFS spectrum. The advantage of this method is the possibility to reconstruct also asymmetric n(r) from the EXAFS spectra. An important parameter in the LI approach is the number of iterations, which determines the reliability of the resulting n(r). We used the L-curve method as described in[30,31] in order to determine the number of iterations. The LI calculated n(r) is shown in Fig. S12 together with the reconstructed EXAFS spectra and FTs. In line with the EXAFS shell fit, n(r) shows only one Pu-O contribution (Fig. S12c). However, Rothe et al.[28] detected two Pu-O contributions with average Pu-O distances of R_{O1} = 2.23 Å and R_{O2} = 2.40 Å, while the difference in these distances (R_{O2}, R_{O1}) of 0.17 Å is close to our radial resolution of 0.14 Å as defined by the used k-range of Δk = 11 Å. Consequently, the ability of the LI approach for resolving such close Pu-O contributions should be tested in order to exclude their presence in our system. For this task we calculated a theoretical model EXAFS spectrum (Fig. S13a) based on EXAFS parameters extracted by the least-squares fit analysis given in Table 2 sample E by Rothe et al.[28] For this sample three shells are given: O1 (R_{O1} = 2.22 Å, CN = 0.7, σ^2 = 0.0012 Å^2), O2 (R_{O2} = 2.38 Å, CN = 5.6, σ^2 = 0.00122 Å^2), and Pu (R = 3.85 Å, CN = 4.3, σ^2 = 0.009 Å^2). Due to the close radial distances of O1 and O2, an asymmetric Pu-O n(r) is obtained (Fig. S13c, black line). The LI was performed by applying the same parameters as used in the case of the experimental spectrum (Pu(IV) at pH >10), i.e.

k-range, k-weighting and number of iterations. The LI calculated Pu-O n(r) (Fig. S13c, red line) is in good agreement with the n(r) of the model, hence if two Pu-O contributions would be present in our system the LI determined n(r) would have an asymmetric shape which is not the case (Fig. S13c).

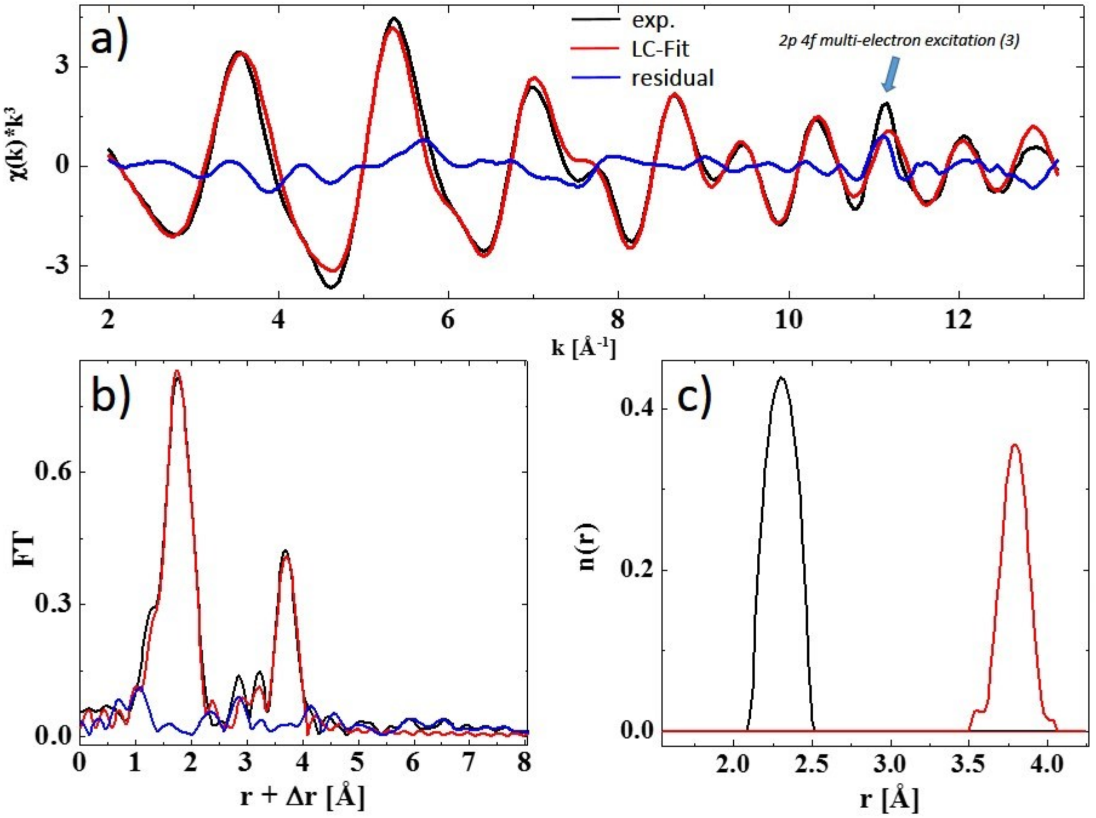

Fig. S12. EXAFS Landweber iteration (LI) for Pu(IV) at pH >10. a) experimental spectrum (black), reconstructed spectrum (red), residual (blue), b) corresponding Fourier transform (FT) magnitude, c) Pu-O (black) and Pu-Pu (red) radial particle distribution function (n(r)).

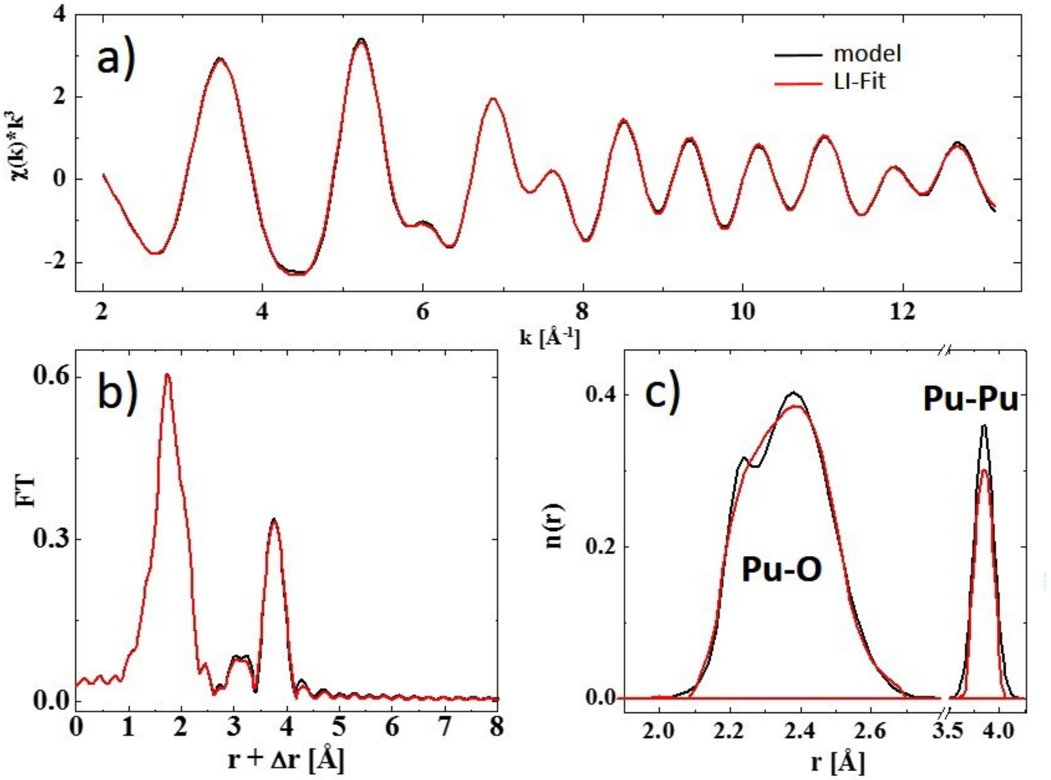

Fig. S13. EXAFS Landweber iteration (LI) for the EXAFS model spectrum. a) model spectrum (black), reconstructed spectrum (red), b) corresponding Fourier transform (FT) magnitude, c) model (black) and LI (red) Pu-O and Pu-Pu radial particle distribution function (n(r)).

We also implemented Monte-Carlo (MC) EXAFS simulations[32–38] as a complementary method to LI. The Metropolis algorithm was included in our MC code as proposed by Gurman et al.[36] For the single scattering (SS) paths the EXAFS kernel (A(k,r)) is calculated with FEFF8.2.0[25] by the method described in[30] and multiple scattering (MS) paths up to the 4th order are calculated during the simulation with a pre-defined spatial precision by FEFF8.2.0.

As a starting structure a PuO_2 cluster with a diagonal length of 14 Å was taken which contains 153 atoms. For the simulation, we used 200 replicas of the PuO_2 cluster. After 20.000.000 atomic movements, i.e. after 650 MC cycles (one cycle corresponds to the number of all atoms), the atomic positions converged to a stationary distribution. After convergence and after each following 10th MC cycle the actual atomic configuration was stored thirty times in order to receive a proper statistical average of n(r).

The MC simulation resulted in a very good agreement with the experimental EXAFS spectrum (Fig. S14a-b) and again the symmetric shape of the first shell Pu-O n(r) is observed (Fig. S14c), thus only one Pu-O contribution is present in our system.

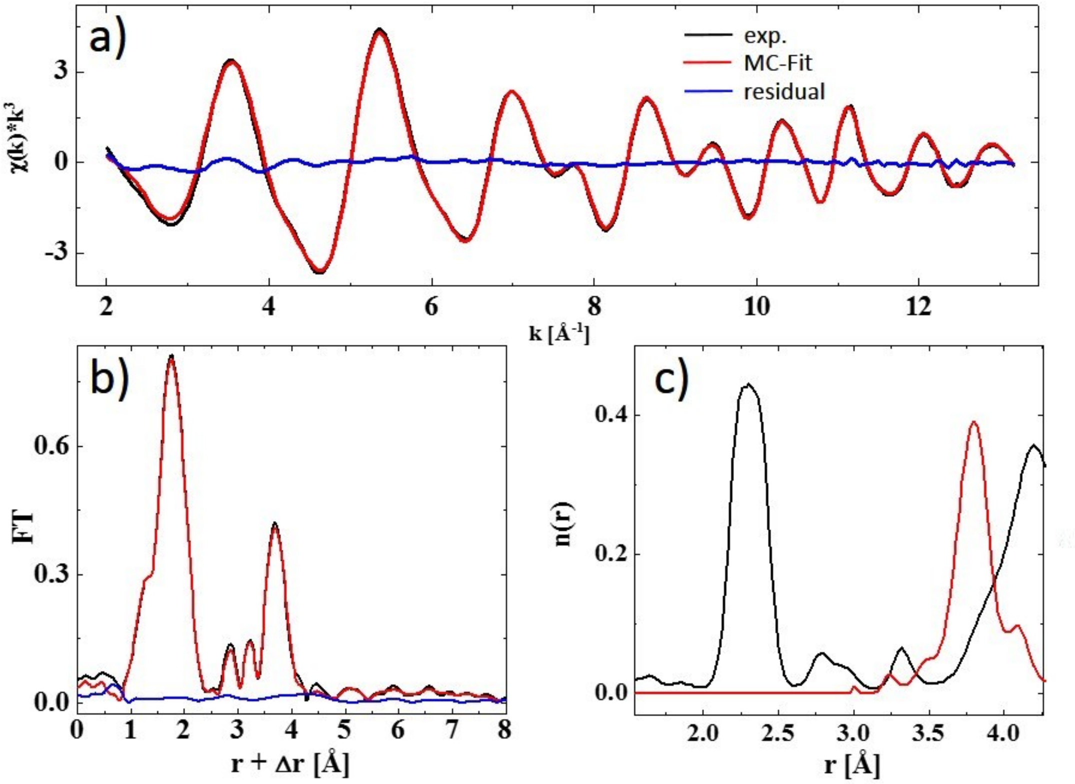

Fig. S14. Monte-Carlo (MC) EXAFS simulation for Pu(IV) at pH >10. a) experimental spectrum (black), reconstructed spectrum (red), residual (blue), b) corresponding Fourier transform (FT) magnitude, c) Pu-O (black) and Pu-Pu (red) radial particle distribution function (n(r)).

Results from HEXS can also clarify the situation. According to the HEXS data (Fig. 2c and d, Fig. S9), there is only one Pu-O contribution with the characteristic distance 2.34 Å, which is in a perfect agreement with the Pu-O distance in the PuO_2 reference structure. The FWHM of the peak is quite large, 0.1-0.2 Å, but the peak is not asymmetric which means that the overlap of two peaks corresponding to the different Pu-O contributions is unlikely for these samples.

Additional information about NP synthesis:

The precipitation process for all samples started shortly (in ten minutes) after adding all reagents. A green precipitate was formed, however, the reaction was continued for about 12 hours to reach equilibrium. Then the pH and redox potential of the precipitation were measured, the results are in Table S5. A Pt electrode relative to an Ag/AgCl reference electrode was used for the redox potential measurement. Eh value was calculated as measured potential (mV) + 208(mV). Due to hydrolysis processes, pH for the samples «from Pu(X) pH >10» was in the range 10-11.5. The electrode potential is higher for samples «from Pu(X) pH 8» and is also increasing with the valence state for these samples.

All sediments «from Pu(X) pH >10» were washed three times with Milli-Q water (18.4 MΩ/cm) to remove the presence of ammonia and samples «from Pu(X) pH 8» were washed once as they already were close to the pH of pure water. To determine the extent of the plutonium precipitation, the following things were done: an aliquot of each suspension was centrifuged (23,900 g, EBA 12 (Hettich)) and the concentration of the Pu in the supernatant was calculated with liquid scintillation spectrometry measurements (Wallac 1414 WIN spectral, PerkinElmer). It was found that for all samples most of the Pu precipitated and was not found in the supernatant.

Table S5. pH and Eh values after the end of the reactions.

Sample	**pH**	**Eh, mV**
from Pu(III) pH >10	10.8	-67
from Pu(IV) pH >10	10.2	-40
from Pu(V) pH >10	11.6	-75
from Pu(III) pH 8	8.0	-5
from Pu(IV) pH 8	8.1	80
from Pu(V) pH 8	8.3	155

References

1 R. G. Haire, M. H. Lloyd, M. L. Beasley and W. O. Milligan, *J. Electron Microsc. (Tokyo).*, 1971, **20**, 8–16.
2 X. Machuron-Mandard and C. Madic, *J. Alloys Compd.*, 1996, **235**, 216–224.
3 P. Thiyagarajan, H. Diamond, L. Soderholm, E. P. Horwitz, L. M. Toth and L. K. Felker, *Inorg. Chem.*, 1990, **29**, 1902–1907.
4 P. K. Smith, G. A. Burney and D. T. Rankin, in *Sixth International Materials Symposium*, 1976.
5 I. R. Triay, D. E. Hobart, A. J. Mitchell, T. W. Newton, M. A. Ott, P. D. Palmer, R. S. Rundberg and J. L. Thompson, *Radiochim. Acta*, 1991, **52–53**, 127–132.
6 C. Ekberg, K. Larsson, G. Skarnemark and I. Persson, *Dalt. Trans.*, 2013, **42**, 2035–2040.
7 A. Y. Romanchuk, T. V Plakhova, A. V Egorov, T. B. Egorova, P. V Dorovatovskii and Y. V Zubavichus, *Dalt. Trans.*, 2018, **47**, 11239–11244.
8 E. Dalodière, M. Virot, V. Morosini, T. Chave, T. Dumas, C. Hennig, T. Wiss, O. Dieste Blanco, D. K. Shuh, T. Tyliszcak, L. Venault, P. Moisy and S. I. Nikitenko, *Sci. Rep.*, 2017, **7**, 1–10.
9 O. Walter, K. Popa and O. D. Blanco, *Open Chem.*, , DOI:10.1515/chem-2016-0018.
10 K. Popa, O. Walter, O. D. Blanco, A. Guiot, D. Bouëxière, J.-Y. Colle, L. Martel, M. Naji and D. Manara, *CrystEngComm*, 2018, **20**, 4614–4622.
11 D. Bouëxière, K. Popa, O. Walter and M. Cologna, *RSC Adv.*, 2019, **9**, 6542–6547.
12 L. Bonato, M. Virot, T. Dumas, A. Mesbah, E. Dalodière, O. Dieste Blanco, T. Wiss, X. Le Goff, M. Odorico, D. Prieur, A. Rossberg, L. Venault, N. Dacheux, P. Moisy and S. I. Nikitenko, *Nanoscale Adv.*, 2020, **2**, 214–224.
13 V. Tyrpekl, J.-F. Vigier, D. Manara, T. Wiss, O. Dieste Blanco and J. Somers, *J. Nucl. Mater.*, 2015, **460**, 200–208.
14 G. I. Nkou Bouala, N. Clavier, J. Léchelle, J. Monnier, C. Ricolleau, N. Dacheux and R. Podor, *J. Eur. Ceram. Soc.*, 2017, **37**, 727–738.
15 D. Hudry, C. Apostolidis, O. Walter, A. Janßen, D. Manara, J. C. Griveau, E. Colineau, T. Vitova, T. Prüßmann, D. Wang, C. Kübel and D. Meyer, *Chem. Eur. J.*, 2014, **20**, 10431–10438.
16 S. Sutherland-harper, F. Livens, C. Pearce, J. Hobbs, R. Orr, R. Taylor, K. Webb and N. Kaltsoyannis, *J. Nucl. Mater.*, , DOI:10.1016/j.jnucmat.2019.02.036.

17 X. Zhou and W. Huebner, *Appl. Phys. Lett.*, 2001, **79**, 3512–3514.

18 J. M. Haschke, T. H. Allen and L. A. Morales, *Science (80-.).*, 2000, **287**, 285–287.

19 V. Neck and J. I. Kim, *Radiochim. Acta*, 2001, **89**, 1–16.

20 A. Tasi, X. Gaona, D. Fellhauer, M. Böttle, J. Rothe, K. Dardenne, D. Schild, M. Grivé, E. Colàs, J. Bruno, K. Källström and M. Altmaier, *Radiochim. Acta*, 2018, **106**, 259–279.

21 J. J. Rehr, J. J. Kas, F. D. Vila, P. P. Micah and K. Jorissen, *Phys. Chem. Chem. Phys.*, 2010, **12**, 5503–5513.

22 B. Ravel and M. Newville, *J. Synchrotron Radiat.*, 2005, **12**, 537–541.

23 T. Ressler, *J. Phys. IV*, 1997, **7**, C2-269.

24 A. Ankudinov and J. Rehr, *Phys. Rev. B - Condens. Matter Mater. Phys.*, 1997, **56**, R1712–R1716.

25 A. Ankudinov and B. Ravel, *Phys. Rev. B - Condens. Matter Mater. Phys.*, 1998, **58**, 7565–7576.

26 R. C. Belin, P. J. Valenza, M. A. Reynaud and P. E. Raison, *Appl. Crystallogr.*, 2004, **37**, 1034–1037.

27 S. D. Conradson, B. D. Begg, D. L. Clark, C. Den Auwer, M. Ding, P. K. Dorhout, F. J. Espinosa-Faller, P. L. Gordon, R. G. Haire, N. J. Hess, R. F. Hess, D. W. Keogh, L. A. Morales, M. P. Neu, P. Paviet-Hartmann, W. Runde, C. D. Tait, D. K. Veirs and P. M. Villella, *J. Am. Chem. Soc.*, 2004, **126**, 13443–13458.

28 J. Rothe, C. Walther, M. A. Denecke and T. Fanghänel, *Inorg. Chem.*, 2004, **43**, 4708–4718.

29 L. Landweber, *Am. J. Math.*, 1951, **73**, 615–624.

30 A. Rossberg and H. Funke, *J. Synchrotron Radiat.*, 2010, **17**, 280–288.

31 P. C. Hansen and D. P. O'Leary, *SIAM J. Sci. Comput.*, 2005, **14**, 1487–1503.

32 A. Rossberg and A. C. Scheinost, *Anal. Bioanal. Chem.*, 2005, **383**, 56–66.

33 M. Winterer, *J. Appl. Phys.*, 2000, **88**, 5635–5644.

34 M. Winterer, R. Delaplane and R. McGreevy, *J. Appl. Crystallogr.*, 2002, **35**, 434–442.

35 M. Winterer and F. Farges, *Phys. Scr.*, 2005, **T115**, 923–924.

36 S. J. Gurman and R. L. McGreevy, *J. Phys. Condens. Matter*, 1990, **2**, 9463–9473.

37 R. L. McGreevy, *J. Phys. Condens. Matter*, 2001, **13**, R877–R913.

38 J. Timoshenko, A. Kuzmin and J. Purans, *Comput. Phys. Commun.*, 2012, **183**, 1237–1245.